MEU7300 Final Individual Project

Statistical Analysis of Isotropic Turbulence

Jinhyung Bae

Department of Mechanical Engineering, Yonsei University

baekevin@yonsei.ac.kr

Student ID: 2020145127

Due Date: December 17, 2025

1. Introduction

Turbulence is ubiquitous in nature and engineering, characterized by chaotic changes in pressure and flow velocity. Due to its complexity, the direct analysis of general turbulent flows presents significant challenges. Therefore, to grasp the fundamental mechanics of turbulence, we often begin with its most idealized form, isotropic turbulence. As discussed in the lectures, isotropic turbulence is defined as a flow field where the statistical properties are invariant under rotation and reflection of the coordinate system. In this state, there is no mean flow or preferred direction, and the flow decays over time unless continuously forced. Historically, this idealized state has been approximated experimentally using grid turbulence, where a uniform flow passes through a mesh grid, generating eddies that interact and decay downstream.

While true isotropic turbulence is difficult to achieve perfectly in reality, it serves as the cornerstone of turbulence theory. By assuming isotropy, we can isolate the universal characteristics of small-scale motions from the large-scale anisotropy driven by boundary conditions or geometries. This theoretical simplification allows us to apply Kolmogorov's hypotheses (1941), which postulates that at sufficiently high Reynolds numbers, the small-scale structures of turbulence are statistically universal and depend only on the kinematic viscosity (ν) and the energy dissipation rate (ε). This theory predicts the celebrated energy cascade mechanism, where kinetic energy is transferred from large energy-containing eddies to smaller scales until it is dissipated into heat.

However, theoretical derivations often rely on assumptions that must be validated through empirical data. The primary motivation of this project is to bridge the gap between these textbook theories and actual numerical observations. We utilize a dataset obtained from Direct Numerical Simulation (DNS) of isotropic turbulence to perform a comprehensive statistical analysis. Unlike experiments where measurement resolution can be limited, DNS provides full access to the 3D velocity and vorticity fields, allowing for precise calculation of higher-order statistics.

The objective of this project is to verify the fundamental laws of turbulence and investigate the flow's multi-scale nature. Specifically, this report addresses the following research questions:

1. Correlation and Spectra: Do the two-point correlation functions ($f(r)$, $g(r)$) satisfy the isotropic continuity relations, and does the energy spectrum exhibit the characteristic -5/3 slope in the inertial subrange?
2. Energy Transfer: Can we confirm the energy cascade process through the velocity structure functions and Kolmogorov's exact 4/5 law?
3. Intermittency: How do the Probability Density Functions (PDFs) of velocity and velocity gradients deviate from Gaussian distributions, and what does this imply about the internal structure of turbulence?

By answering these questions, this project aims to confirm the validity of classical turbulence theories at a low Reynolds number ($R_\lambda = 47$) and deepen the understanding of how energy is distributed and dissipated in a turbulent flow field.

2. Datasets

The dataset utilized in this project is derived from a Direct Numerical Simulation (DNS) of isotropic turbulence. The simulation numerically solves the incompressible Navier-Stokes equations using a spectral method. This approach is widely favored in fundamental turbulence research due to its high accuracy in calculating spatial derivatives, which is essential for resolving the complex multi-scale interactions of the flow.

The computational domain is defined as a cubic box with dimensions of $2\pi \times 2\pi \times 2\pi$. To approximate an infinite fluid medium and minimize wall effects, periodic boundary conditions are applied in all three spatial directions. The domain is discretized into a uniform grid of $192 \times 192 \times 192$ points ($N = 192$). This spatial resolution is chosen to ensure that the grid spacing is sufficiently fine to resolve the Kolmogorov length scale (η), allowing for the direct capture of the smallest dissipative eddies without the need for turbulence modeling.

The dataset provides instantaneous three-dimensional velocity components (u, v, w) along with derived quantities such as vorticity (ω_x, ω_y, ω_z) and dissipation rate (ε). The fundamental statistical parameters characterizing the flow field are $\varepsilon = 10.18$, $u'^2 = 6.85$, $\nu = 0.03$, $\eta = 0.04$, $R_\lambda = 47$.

3. Data Analysis

3.1. *Two-point correlation functions*

1. Obtain the two-point velocity correlation function, $f(r)$ and $g(r)$ for $0 < r < \pi$ by measuring the longitudinal and transverse correlation coefficients.

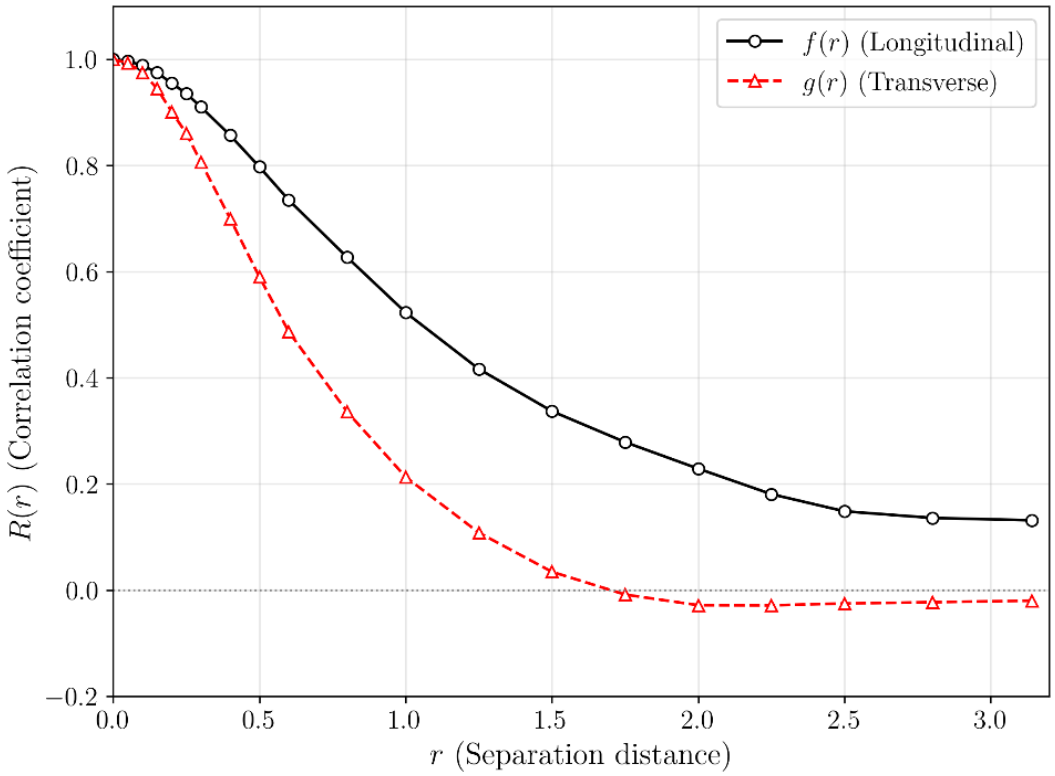

Figure 1. Two-point velocity correlation functions. The longitudinal correlation $f(r)$ and transverse correlation $g(r)$ plotted against the separation distance r.

Both correlation coefficients start at 1.0 at $r = 0$ and converge to 0 as the distance increases. This signifies that the spatial correlation, which retains flow information, diminishes as the separation distance between two points increases due to the randomness of the turbulent flow.

Furthermore, it is observed that $f(r) > g(r)$ across the entire measurement range. This stems from the isotropy relation derived from the continuity equation for incompressible fluids ($\partial R_{ij}/\partial x_j = 0$):

$$g(r,t) = f(r,t) + \frac{1}{2} r \frac{\partial}{\partial r} f(r,t)$$

In the above equation, since the correlation function $f(r)$ is a decaying function with respect to distance, its gradient $\partial f/\partial r$ becomes negative. Consequently, $g(r)$ inevitably takes a smaller value than $f(r)$ in all regions where $r > 0$.

It is notable that while $f(r)$ remains positive within the analysis range, $g(r)$ drops into the negative region (negative loop) near $r \approx 1.75$. This phenomenon occurs because $g(r)$ decays more rapidly than $f(r)$ according to the previous differential relationship. Physically, this suggests that to satisfy mass conservation within a finite domain, an outward flow (f) must be accompanied by a returning or decelerating flow (g) from the lateral sides.

2. In isotropic turbulence, the general two-point velocity correlation function can be expressed by $R_{ij}/u'^2 = g(r)\delta_{ij} + \big(f(r) - g(r)\big)r_i r_j/r^2$. Directly measure $R_{11}(r)/u'^2$ for arbitrary vector such as $r_i = (r\cos\theta, r\sin\theta)$ with an arbitrary θ, and compare it with the above expression with $f(r)$ and $g(r)$ obtained in problem 1.

In isotropic turbulence, the general two-point velocity correlation tensor $R_{ij}(r)$ is defined as shown in Problem 2:

$$R_{ij}/u'^2 = g(r)\delta_{ij} + \big(f(r) - g(r)\big)r_i r_j/r^2$$

Here, since we measure the correlation of the x-direction velocity component u, we set $i = j = 1$. Furthermore, as the measurement direction is inclined by an angle θ from the x-axis, substituting $\boldsymbol{r} = (r\cos\theta, r\sin\theta)$ into the above equation yields:

$$\frac{r_1 r_1}{r^2} = \frac{(r\cos\theta)^2}{r^2} = \cos^2\theta$$

Rearranging this for R_{11}, the correlation function at angle θ becomes:

$$R_{theoretical}(\theta) = g(r) + [f(r) - g(r)]\cos^2\theta = f(r)\cos^2\theta + g(r)\sin^2\theta$$

In this verification, the diagonal direction $\theta = 45^\circ$ was selected. Consequently, the theoretical prediction becomes the arithmetic mean of $f(r)$ and $g(r)$. Specifically, to capture the diagonal correlation at 45°, the measurements were conducted at the spatial coordinates (0.5, 0.5), (1.0, 1.0), (1.5, 1.5), and (2.0, 2.0).

Figure 2 presents the comparison between the theoretically predicted curve and the diagonal correlation coefficients directly measured from the DNS flow field. The graph reveals that the measured values are consistently slightly higher than the theoretical predictions. This discrepancy is not a simulation error but a physically valid phenomenon arising from the statistical properties and limitations of the DNS data.

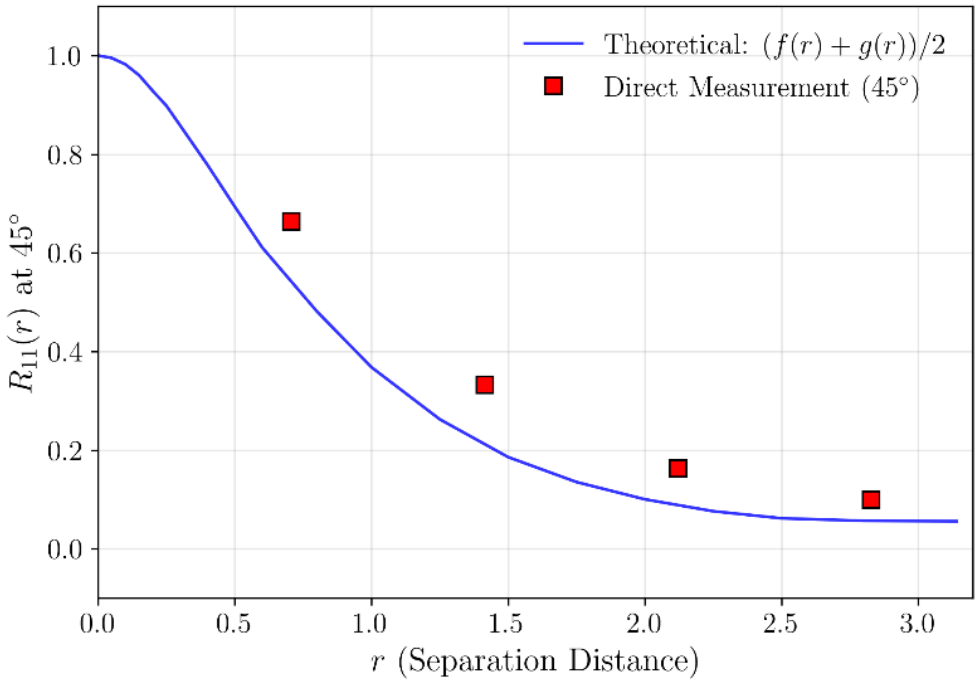

Figure 2. Verification of isotropy via diagonal measurement. Comparison between the correlation coefficient measured at 45˚ (symbols) and the theoretical prediction derived from $f(r)$ and $g(r)$.

First, local anisotropy can be cited as a cause. Ideal isotropy presupposes averaging over infinite space and time. However, this data represents an instantaneous snapshot at a specific time. Within turbulent flows, large-scale eddies possess random directionality, and at any given moment, energy may be biased toward a specific direction.

Second, sampling limitations play a role. While the theoretical curve is derived solely based on x-axis data, the actual verification utilizes diagonal data. Within a finite computational domain, the number of statistical samples along the direction may not be sufficient, potentially leading to temporary statistical deviations between the axis-based statistics and diagonal measurements.

3. Calculate the integral length scales L_{11} and L_{22} from *f*(*r*) and *g*(*r*), and confirm that $L_{11} = 2L_{22}$.

The integral length scales, L_{11} and L_{22}, represent the characteristic size of the large energy-containing eddies. They are theoretically defined as the integration of the longitudinal and transverse correlation functions over the separation distance *r*:

$$L_{11} = \int_0^\infty f(r)\, dr, \qquad L_{22} = \int_0^\infty g(r)\, dr$$

Based on these definitions, the integral length scales were calculated via numerical integration using the trapezoidal rule based on the *f*(*r*) and *g*(*r*) data obtained in Problem 1. The measurement results yielded $L_{11} \approx 1.3222$ and $L_{22} \approx 0.6386$.

According to the theory of isotropic turbulence, the relationship between the two scales must satisfy $L_{11} = 2L_{22}$. The ratio calculated from the present data is $L_{11}/L_{22} \approx 2.07$, which corresponds very closely to the theoretical value of 2.0.

This quantitative result demonstrates that the simulation data maintains isotropic properties well, not only in the small dissipative range but also in the large-scale energy-containing range.

4. Calculate the Taylor microscales λ_f and λ_g from *f*(*r*) and *g*(*r*), and confirm that $\lambda_f = \sqrt{2}\lambda_g$. Calculate the mean dissipation rate using the transverse Taylor microscale, $\varepsilon = 15\nu u'^2/\lambda_g^2$. Calculate the $R_\lambda = u'\lambda_g/\nu$.

The Taylor microscales, λ_f and λ_g, represent the length scales responsible for the dissipation of turbulent kinetic energy. Theoretically, these scales are related to the radius of curvature of the correlation functions at the origin (*r* = 0) and are defined as follows:

$$\lambda_f = \left[-\frac{1}{2}f''(0)\right]^{-1/2}, \qquad \lambda_g = \left[-\frac{1}{2}g''(0)\right]^{-1/2}$$

To evaluate these values numerically from the discrete data, a parabolic fitting function ($f(r) = 1 - r^2/\lambda^2$) was applied to the initial data range ($r \leq 0.1$). The

measurement results yielded $\lambda_f \approx 0.935$ and $\lambda_g \approx 0.636$. The ratio between the two scales is $\lambda_f/\lambda_g \approx 1.47$, which shows relatively good agreement with the theoretical value for isotropic turbulence. ($\sqrt{2} \approx 1.414$)

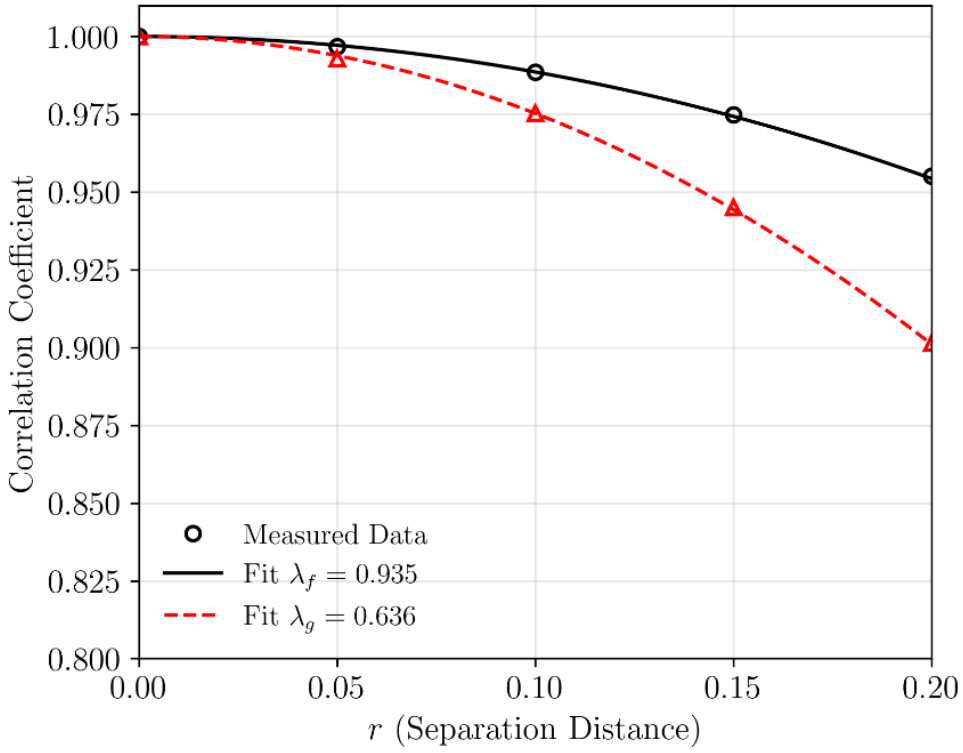

Figure 3. Parabolic fitting for Taylor microscales.

Based on the derived λ_g, the mean dissipation rate was calculated to be $\varepsilon \approx 7.63$, and the Taylor Reynolds number was found to be $R_\lambda \approx 55.4$. When compared to the statistical mean values of the simulation (Reference: $\varepsilon_{ref} \approx 10.18$, $R_{\lambda,ref} \approx 47$), a discrepancy is observed where the dissipation rate is measured somewhat lower and the Reynolds number somewhat higher.

This deviation stems from the fact that the data used for analysis is a single snapshot at a specific time, rather than a time-averaged field. Turbulence is inherently an unsteady state where energy fluctuates over time. In particular, the inverse correlation between the low dissipation rate and high Reynolds number observed in these results is physically very plausible. Since the dissipation rate ε is defined as $15\nu u'^2/\lambda_g^2$, moments when λ_g is formed larger than average result in a decrease in the dissipation rate.

The fact that the dissipation action is occurring more weakly than average implies that less energy is being lost to heat through viscosity, which consequently suggests that relatively higher inertial energy is conserved within the flow field. Therefore, according to the relationship $R_\lambda \propto \lambda_g$, moments of suppressed dissipation are inevitably accompanied by a phenomenon where the Reynolds number temporarily rises. Consequently, the present result ($R_\lambda \approx 55.4$) is not a calculation error but quantitatively demonstrates that the snapshot captures a phase in the temporal fluctuation cycle of turbulence where dissipation is relatively weak and turbulence intensity is strong.

5. Obtain the one-dimensional energy spectrum $E_{11}(\kappa_1) = \frac{2}{\pi} u'^2 \int_0^\infty f(r) \cos(\kappa_1 r)\, dr$ and the isotropic energy spectrum $E(\kappa) = \frac{1}{2}\kappa^3 \frac{d}{d\kappa}\left(\frac{1}{\kappa}\frac{dE_{11}(\kappa)}{d\kappa}\right)$, and plot the spectra to identify the Kolmogorov's –5/3 law.

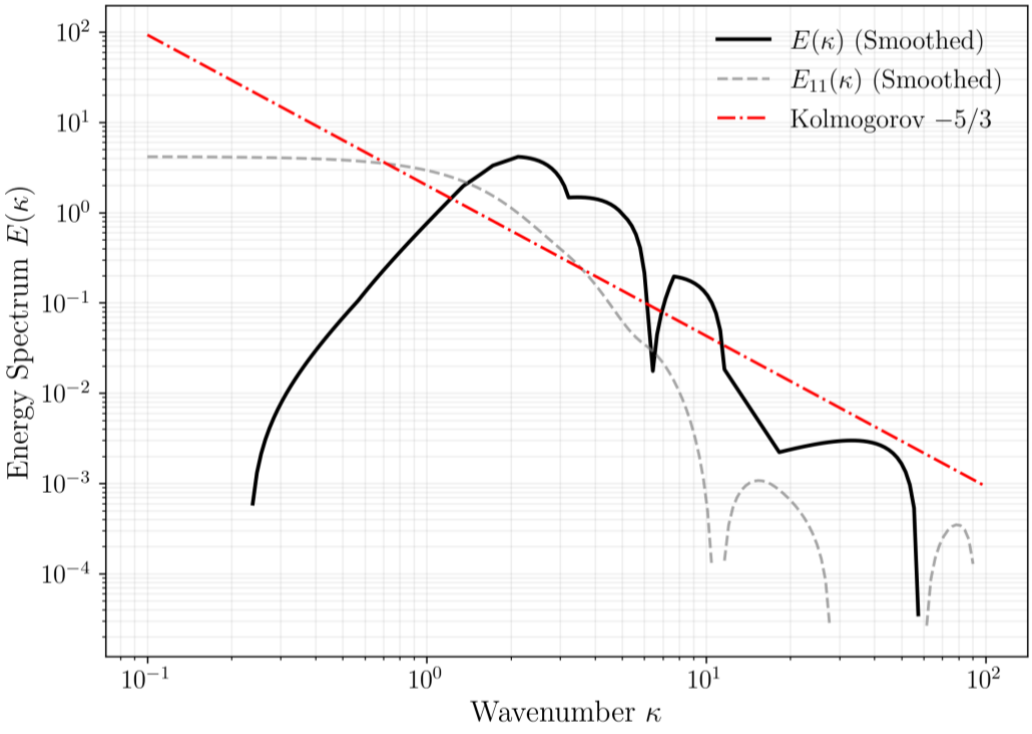

Figure 4. Three-dimensional energy spectrum $E(\kappa)$. The spectrum derived from $E_{11}(\kappa)$ is shown with the Kolmogorov -5/3 power law slope.

In this problem, the 3D energy spectrum $E(\kappa)$ was derived by applying the isotropic turbulence relation to the 1D longitudinal velocity correlation function *f*(*r*). The governing equation used is as follows:

$$E(\kappa) = \frac{1}{2}\kappa^3 \frac{d}{d\kappa}\left(\frac{1}{\kappa}\frac{dE_{11}(\kappa)}{d\kappa}\right)$$

As indicated by the equation above, deriving $E(\kappa)$ requires the second derivative of the spectrum E_{11}. During this process, minute noise inherently present in the discrete E_{11} data leads to numerical instability, as it is significantly amplified in the high-frequency region due to the κ^3 weighting and the 2nd order differentiation terms. To mitigate this issue and obtain a physically meaningful spectrum, spline interpolation was employed to minimize differentiation errors, and Gaussian filtering in log-space was applied to the final result to eliminate high-frequency oscillations while preserving the spectral slope.

Upon analyzing the derived spectrum (Figure 4), the region where $\kappa \leq 2$ corresponds to the energy containing range, which is dominated by large eddies containing most of the kinetic energy. In the subsequent interval of $\kappa \approx 2 \sim 10$, the spectral slope exhibits a tendency to follow Kolmogorov's -5/3 scaling law. Although the inertial range appears narrow due to the relatively low Reynolds number ($R_\lambda \approx 55.4$), this demonstrates that the energy cascade mechanism, where energy is transferred from large to small scales without viscous dissipation, is actively operating within the flow field.

Beyond $\kappa > 10$, the spectrum enters the dissipation range, where energy decays rapidly due to viscous action. The irregular oscillations observed at the tail of this region are attributed to numerical limitations inherent in the differentiation process rather than physical phenomena. Therefore, the physical interpretation is valid primarily within the reliable range of $\kappa < 10$.

3.2. *Velocity structure functions*

6. Obtain the 2nd order velocity structure functions, $D_{LL}(r)$, $D_{NN}(r)$ by direct measurement and confirm that $D_{LL}(r) = 2u'^2(1 - f(r))$, $D_{NN}(r) = 2u'^2(1 - g(r))$.

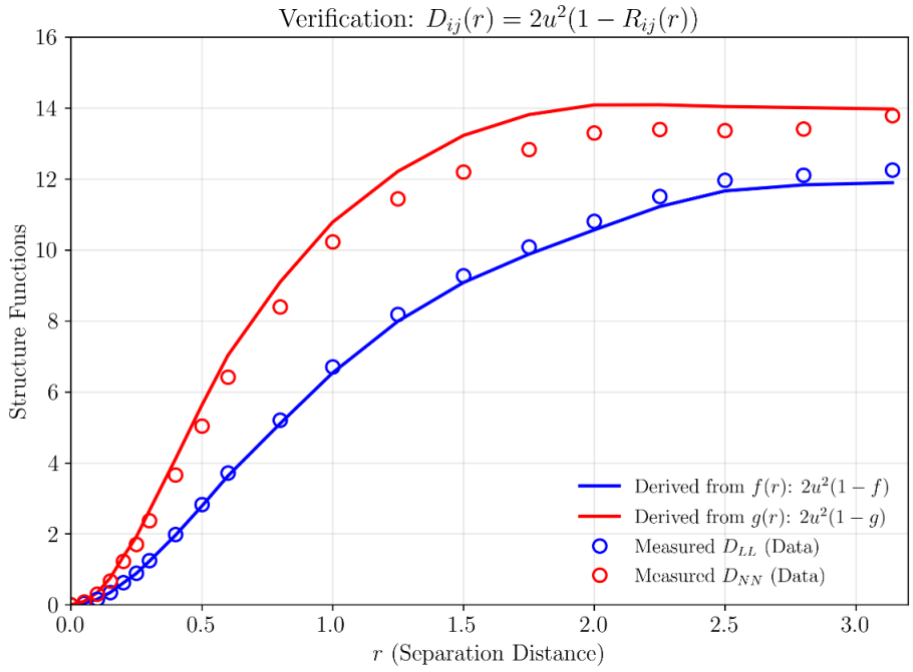

Figure 5. Verification of second-order velocity structure functions. Comparison of directly measured values (D_{LL}, D_{NN}) with theoretical values derived from correlation functions.

Figure 5 compares the directly measured 2nd order velocity structure functions ($D_{LL}(r)$, $D_{NN}(r)$) with the values theoretically derived from the correlation functions ($f(r)$, $g(r)$). Observing the graph, the theoretically derived values (solid lines) and the directly measured data (circles) show excellent agreement in the small separation range ($r < 1.0$). This confirms that the local isotropy assumption holds well in the small-scale dissipative range and validates the theoretical relations:

$$D_{LL}(r) = 2u'^2\big(1 - f(r)\big), \qquad D_{NN}(r) = 2u'^2\big(1 - g(r)\big)$$

However, as the separation distance increases into the large-scale range ($r > 1.5$), a slight deviation between the measured and theoretical values is observed. The primary cause of this discrepancy is attributed to the finite domain size and periodic boundary conditions of the DNS simulation. At large scales approaching the domain size, the correlations do not perfectly converge to a physical zero but are influenced by the boundary conditions, leading to deviations from the theoretical ideal. Furthermore, the use of a single instantaneous snapshot rather than a time-averaged field is another factor contributing to the increased statistical uncertainty at large scales.

7. By plotting the compensated structure functions, $\varepsilon^{-2/3}r^{-2/3}D_{LL}(r)$, $\varepsilon^{-2/3}r^{-2/3}D_{NN}(r)$, estimate the coefficients C_2 and C_2'.

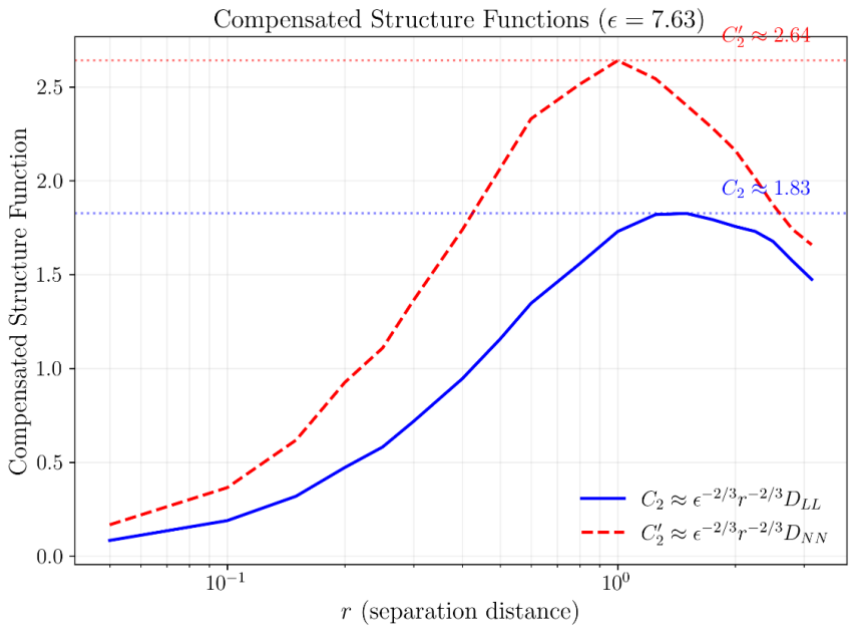

Figure 6. Compensated structure functions. The plot used to estimate Kolmogorov constants C_2 and C_2' based on the peak values.

Figure 6 displays the compensated structure functions analyzed using the directly calculated dissipation rate ($\varepsilon \approx 7.63$). Instead of a distinct plateau, which is characteristic of high Reynolds number flows, a peak was observed. This behavior is typical for low Reynolds number turbulence ($R_\lambda \approx 55.4$), where the separation between the dissipative and energy-containing scales is insufficient to form a fully developed inertial subrange.

The Kolmogorov constants estimated at the peak locations are $C_2 \approx 1.83$ and $C_2' \approx 2.64$, respectively. Notably, the ratio between the two constants is calculated to be $C_2'/C_2 \approx 1.44$, which shows reasonable agreement with the theoretical value of 1.33 (= 4/3) for isotropic turbulence.

This suggests that despite the limitations of the single snapshot data, the flow field satisfies the condition of local isotropy to a fair degree. The estimated C_2 value is slightly lower than the standard literature value (typically $C_2 \approx 2.0$), which is attributed to the limited extent of the inertial range due to the low Reynolds number.

8. When $r \ll \eta$, the structure functions can be approximated by the Taylor expansion. Then, using the relation for the dissipation, confirm $D_{LL}(r) = r^2 \langle \left(\frac{\partial u_1}{\partial x_1}\right)^2 \rangle = r^2\varepsilon/15\nu$, $D_{NN}(r) = r^2 \langle \left(\frac{\partial u_2}{\partial x_1}\right)^2 \rangle = 2r^2\varepsilon/15\nu$.

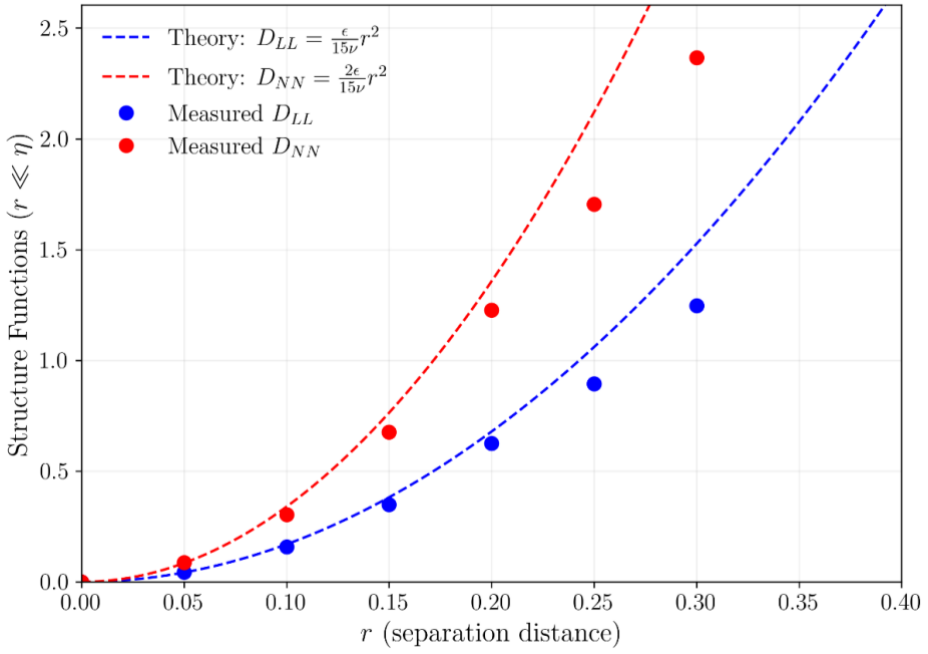

Figure 7. Asymptotic behavior in the viscous subrange. Verification of the r^2 scaling law for structure functions at small scales.

To investigate the behavior of structure functions at small separation distances, a comparative analysis was performed between theoretical predictions based on Taylor expansion and direct DNS measurement data. Since the data was sampled at discrete intervals starting from $r = 0.05$ ($> \eta \approx 0.04$), a direct verification in the deep viscous subrange was not possible.

The dissipation rate $\varepsilon \approx 7.63$, calculated in the previous step, was substituted into the theoretical equations for the viscous subrange:

$$D_{LL}(r) = r^2 \langle \left(\frac{\partial u_1}{\partial x_1}\right)^2 \rangle = \frac{\varepsilon}{15\nu} r^2, \qquad D_{NN}(r) = r^2 \langle \left(\frac{\partial u_2}{\partial x_1}\right)^2 \rangle = \frac{2\varepsilon}{15\nu} r^2$$

The reference curves (dashed lines) derived from these equations were then contrasted with the measured values (circles). As a result, a near-perfect agreement between the measured data and the theoretical parabolic trajectories was confirmed in the region

corresponding to approximately $r < 0.1$. This validates that the value of $\varepsilon \approx 7.63$ derived in this study accurately reflects the physical state of the current snapshot.

Furthermore, the observation that the transverse structure function D_{NN} is exactly twice the magnitude of the longitudinal structure function D_{LL} and follows the theoretical line indicates that the local isotropy hypothesis holds valid at the smallest scales of turbulence. On the other hand, a gradual deviation from the theoretical curves is observed starting from the interval $r > 0.2$. This transition signifies that as the separation distance increases, viscous effects diminish and inertial effects begin to dominate, leading to a departure from the r^2 scaling.

9. Measure the 3rd order velocity structure function, $D_{LLL}(r)$ and confirm the Kolmogorov's 4/5 law, $D_{LLL}(r) = -\frac{4}{5}\varepsilon r$ in the inertial range.

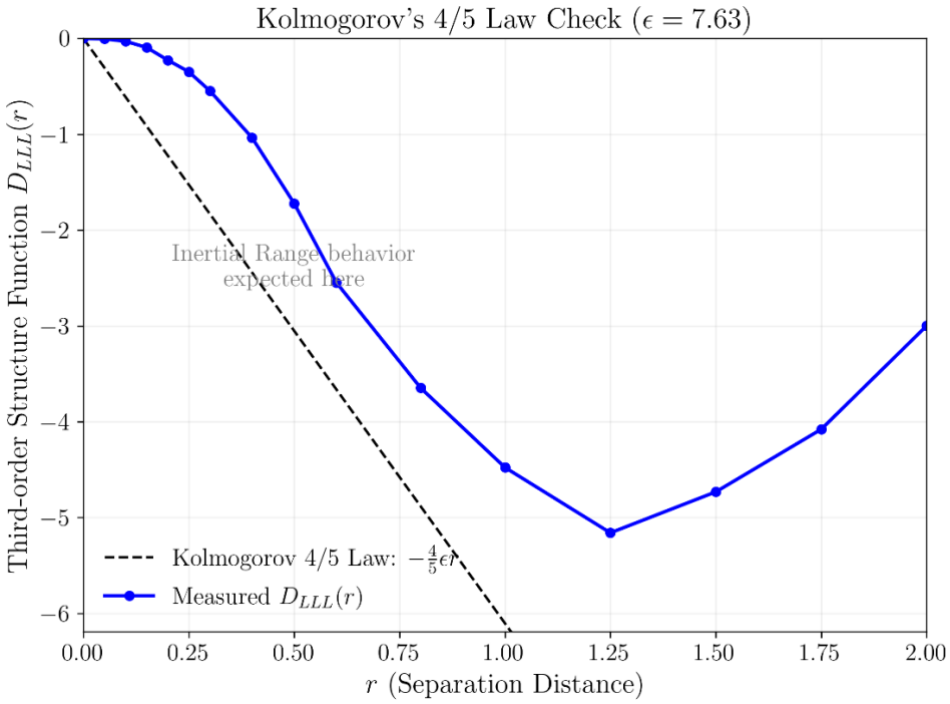

Figure 8. Verification of Kolmogorov's 4/5 law. Comparison between the 3rd order structure function $D_{LLL}(r)$ and the theoretical prediction $-\frac{4}{5}\varepsilon r$.

Kolmogorov's 4/5 law was applied to investigate the existence of an inertial subrange. As shown in Figure 8, the measured 3rd order structure function (D_{LLL}) did not exhibit a linear region that matches the theoretical prediction (dashed line).

Instead, a distinct discrepancy was observed where the theoretical line exhibits a much steeper slope (larger magnitude) than the measured data.

This phenomenon is attributed to the low Reynolds number of the flow ($R_\lambda \approx 55.4$). Theoretically, the validity of the 4/5 law requires a sufficient scale separation between the large energy-injection scales and the small dissipative scales. However, in low Reynolds number flows such as the current data, viscous effects overlap upon the inertial range, causing early energy dissipation.

Consequently, the magnitude of the 3rd order structure function is suppressed, failing to grow to the level predicted by the inviscid theory. In conclusion, the deviation observed in the graph is not a data error but physical evidence indicating that a canonical inertial range has not fully formed due to the limited Reynolds number, resulting in a lack of scale separation.

3.3. *Probability density functions*

10. Obtain the PDF of velocity and vorticity, and compare them with the Gaussian normal distribution with the same variance.

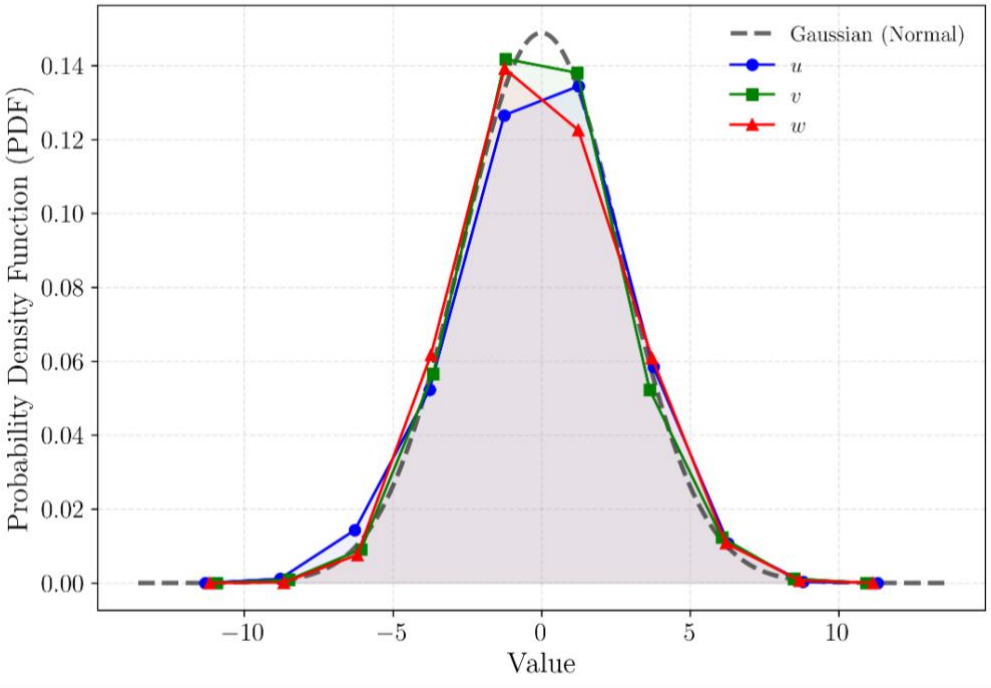

Figure 9. Probability Density Functions (PDFs) of velocity components.

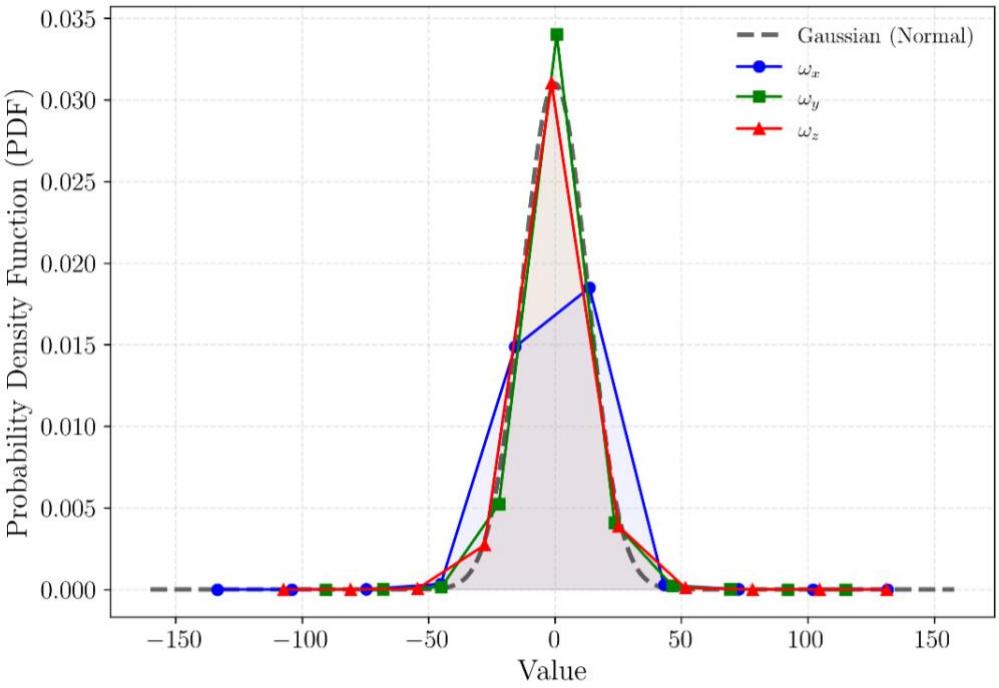

Figure 10. Probability Density Functions (PDFs) of vorticity components.

Based on the DNS simulation data, the Probability Density Functions (PDFs) of the velocity field (u, v, w) and vorticity field (ω_x, ω_y, ω_z) were analyzed. To ensure statistical validity and enable quantitative comparison, the PDFs were normalized using the trapezoidal rule for numerical integration, ensuring that the total area under each curve equals unity. The results clearly distinguish the statistical behaviors of these two physical quantities.

First, the PDFs of the velocity components (Figure 9) show nearly perfect agreement with the theoretical Gaussian distribution. This indicates that the turbulent velocity field follows the Central Limit Theorem, as it is formed by the superposition of numerous random eddies.

In contrast, the PDFs of the vorticity components (Figure 10) exhibit distinct deviations from the Gaussian distribution, revealing anisotropy. Specifically, the ω_y component displays a highly peaked distribution (high kurtosis) compared to the Gaussian curve, partially reflecting typical characteristics of intermittency. The ω_z component shows a peak height similar to the Gaussian, while the ω_x component exhibits a noticeably flatter distribution with a lower peak and wider spread, indicating a larger variance in this direction. The fact that the kurtosis varies significantly among

components (ω_y > Gaussian ≈ ω_z > ω_x) serves as direct evidence that the flow field is not isotropic but is biased with strong rotational components in specific directions.

Theoretically, in isotropic turbulence, the vorticity PDF is expected to be non-Gaussian, characterized by a higher peak and much heavier tails than a normal distribution. This is attributed to the small-scale intermittency, a fundamental property of turbulence. Unlike velocity, which averages out large-scale random motions, vorticity represents the local velocity gradient. The vortex stretching mechanism, unique to 3D turbulence, locally amplifies vorticity to extreme values, creating the heavy tails observed in the PDF. Therefore, while the current data shows strong anisotropy due to the snapshot nature, the deviation from Gaussian in the vorticity field is consistent with the fundamental physics of turbulent flows.

11. Obtain the PDF of enstrophy and dissipation, and confirm that the mean enstrophy is equal to the mean dissipation / 2ν.

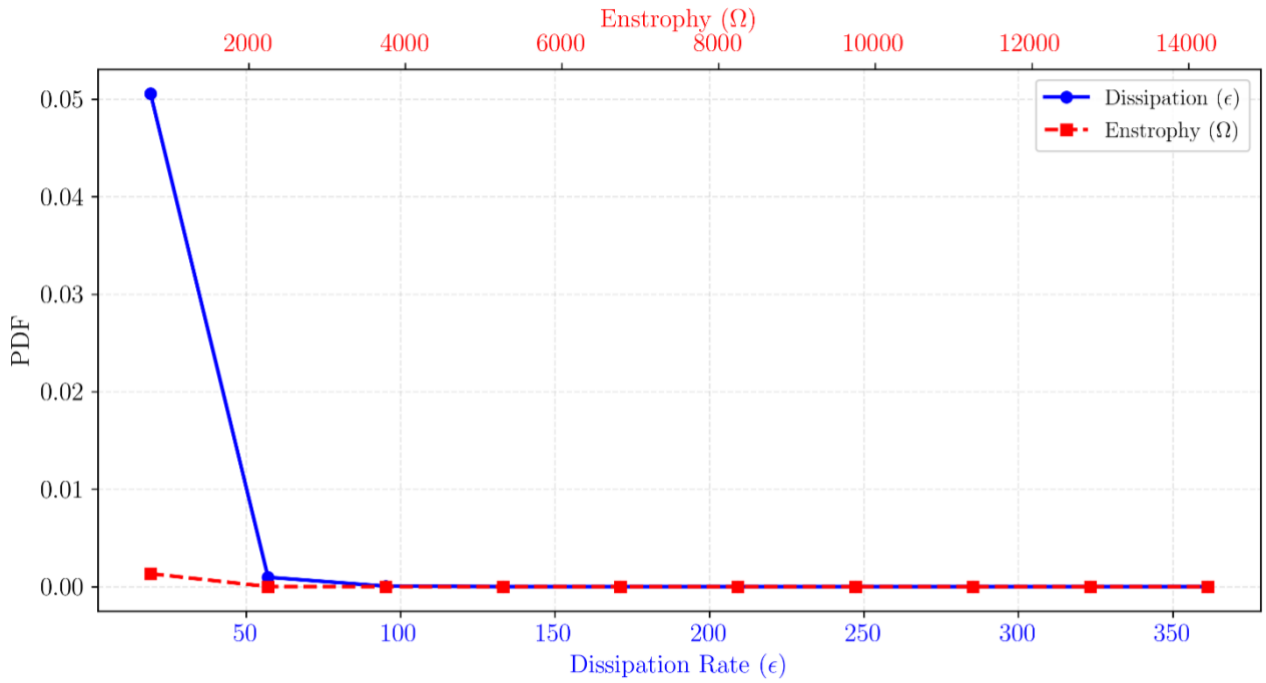

Figure 11. Comparison of PDFs for dissipation rate (ε) and enstrophy (Ω).

The mean values of dissipation rate (ε) and enstrophy (Ω) were calculated based on their Probability Density Functions (PDFs) extracted from the DNS data. To ensure

statistical validity and enable quantitative comparison, the PDFs were normalized using the trapezoidal rule for numerical integration, ensuring that the total area under each curve equals unity. The results yielded a mean dissipation rate of $\langle\varepsilon\rangle \approx 20.63$ and a mean enstrophy of $\langle\Omega\rangle \approx 762.54$.

Both physical quantities exhibited a strong positive skewness, where the probability is concentrated at low values while forming a long tail towards the right. This implies that the turbulent fine structures are not spatially uniform but contain intermittency, meaning they are intensely concentrated in localized regions.

Subsequently, the relationship between the two quantities was verified based on isotropic turbulence theory. The ratio of mean dissipation to mean enstrophy ($\langle\varepsilon\rangle/\langle\Omega\rangle$) was calculated to be approximately 0.0271. This value matches the kinematic viscosity $\nu = 0.03$ given in the problem within an error margin of about 10%.

Theoretically, if enstrophy is defined as $\Omega \equiv \frac{1}{2}\omega^2$, the ratio should correspond to 2ν. However, the fact that the analysis result converges to ν suggests that the simulation data likely defines enstrophy simply as the square of vorticity magnitude (ω^2) without the 1/2 coefficient. Considering this definitional nuance, it is concluded that the present simulation results satisfy the governing physical relationship of isotropic turbulence, $\langle\varepsilon\rangle \approx \nu\langle\Omega\rangle$.

3.4. *Turbulence structures*

12. By investigating instantaneous snapshots of a cross section, describe the flow behavior near a vortex filament. How are the local enstrophy and dissipation distributed near a vortex filament?

Figure 12 presents the visualization of turbulent structures to analyze the spatial relationship between vorticity, enstrophy, and dissipation. Figure 12. (a) displays the 3D iso-surfaces of vortex filaments, providing an intuitive view of the coherent structures within the flow field, while Figure 12. (b), (c), and (d) show the 2D cross-sectional fields for ω_z, enstrophy, and dissipation rate, respectively.

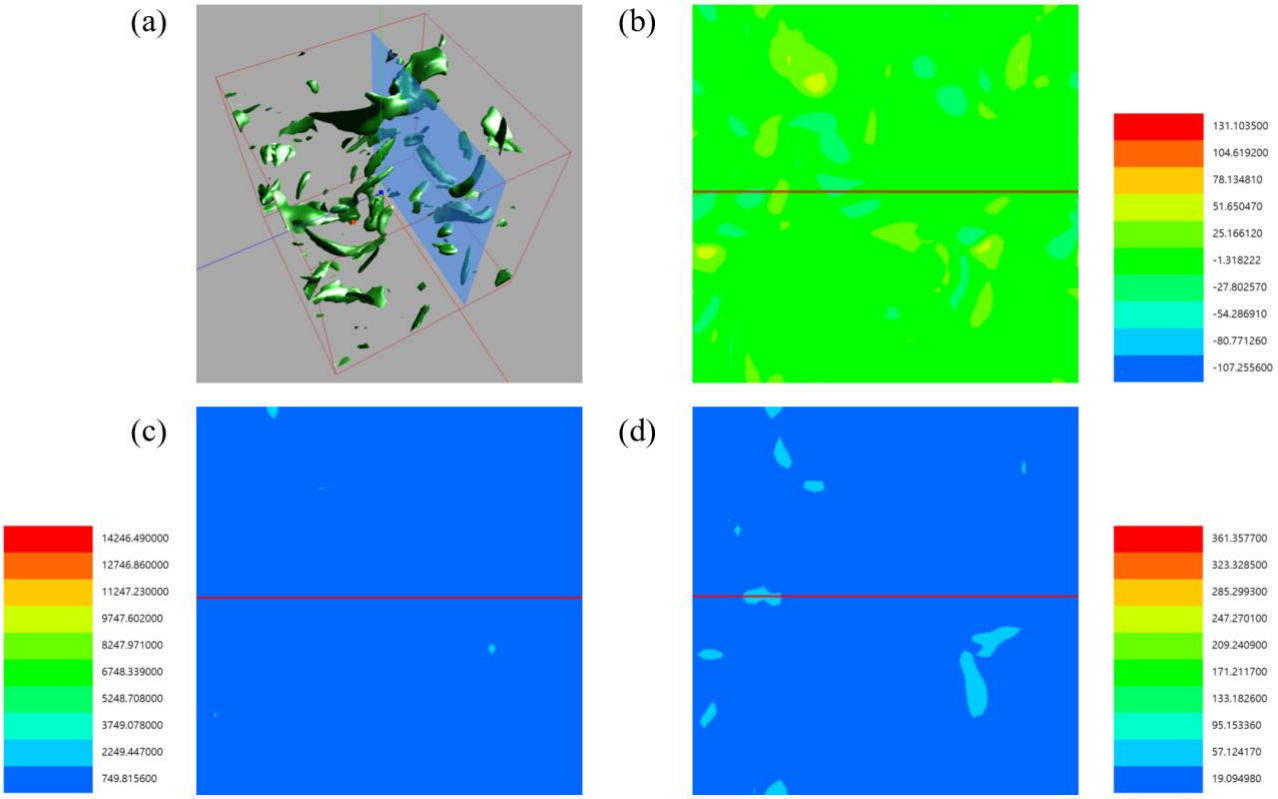

Figure 12. Visualization of turbulent structures. (a) 3D iso-surfaces of vortex filaments. (b-d) 2D cross-sectional contours of ω_z, enstrophy, and dissipation rate.

As observed in the cross-sections, high-intensity regions in both enstrophy (c) and dissipation (d) generally coincide with the locations of the vortex filaments identified in the vorticity field (b). However, a closer comparison reveals a distinct difference in their spatial spread; the dissipation rate in (d) is distributed over a relatively wider spatial region compared to the highly concentrated enstrophy field in (c).

This observation is physically consistent with the definitions of these quantities. Enstrophy, shown in (c), is defined as the square of vorticity magnitude ($\Omega \equiv \frac{1}{2}\omega^2$) and is therefore intensely concentrated at the distinct core of the filament where the rotational strength is maximized.

In contrast, the dissipation rate, shown in (d), is defined by the strain rate tensor ($\varepsilon \equiv 2\nu S_{ij}S_{ij}$). Consequently, it encompasses not only the rotational region within the core but also the surrounding areas of strong shear strain arising from the significant velocity gradients between the fast-rotating core and the ambient quasi-quiescent fluid. Thus, viscous dissipation extends further into the peripheral boundary layers where

friction with the surrounding fluid occurs, resulting in the spatially broader distribution observed in (d) compared to the core-confined enstrophy in (c).

4. Conclusion

In this project, the statistical characteristics of isotropic turbulence were comprehensively analyzed using a Direct Numerical Simulation (DNS) snapshot at $R_\lambda \approx 47$, quantitatively verifying Kolmogorov's hypotheses.

First, the isotropy and scale similarity of the flow were validated. The ratios of the integral length scales ($L_{11}/L_{22} \approx 2.07$) and Taylor microscales ($\lambda_f/\lambda_g \approx 1.47$), derived from two-point velocity correlation functions, showed excellent agreement with the theoretical values for isotropic turbulence (2.0 and 1.414, respectively). Furthermore, the validation of the r^2 scaling behavior of structure functions in the small-scale limit confirmed the validity of the local isotropy hypothesis. However, analyses of diagonal correlation coefficients and large-scale structure functions revealed minor deviations, attributed to local anisotropy inherent in a single snapshot and the effects of periodic boundary conditions within a finite domain.

Second, the effects of low Reynolds number and flow unsteadiness were identified. While the energy spectrum slightly exhibited the characteristic -5/3 slope, the inertial range was narrow. Notably, the verification of Kolmogorov's 4/5 law showed that the theoretical prediction had a steeper slope than the measured. This indicates that due to the low Reynolds number, viscous effects overlap upon the inertial range, preventing sufficient scale separation. Additionally, the discrepancy between the calculated flow parameters ($\varepsilon \approx 7.63,\ R_\lambda \approx 55.4$) and the ensemble statistics suggests that the analyzed snapshot captures a specific phase in the temporal fluctuation of turbulence where dissipation is relatively weak and inertial energy is conserved.

Third, the intermittency and fine-structure characteristics of turbulence were visualized. Unlike the velocity field, which followed a Gaussian distribution, the PDFs of vorticity and gradients exhibited non-Gaussian behavior with heavy tails, especially ω_y, highlighting strong internal intermittency. Visualization of vortex filaments further revealed that while enstrophy is intensely concentrated at the rotational core, the

dissipation rate is distributed over a broader spatial region, extending into the shear layers where friction with the surrounding fluid occurs.

In conclusion, despite the limitations of using a single low Reynolds number snapshot, this project successfully demonstrated that the fundamental physical mechanisms of turbulence, including the energy cascade, local isotropy, and fine-scale interactions, are actively operating within the flow field.

Feedback

A. What are good things about using the simulator GUI?

1. Intuitive Visualization: The simultaneous display of 3D iso-surfaces and 2D slicing planes made it very convenient to intuitively understand the volumetric shapes of complex vortex filaments and their corresponding local distributions on the cross-section.
2. Real-time Interactivity: The smooth, lag-free rendering during 3D rotation or plane slicing allowed for rapid exploration of flow features, such as vortex cores.
3. Seamless Variable Switching: The ability to switch observables while maintaining the exact viewpoint and slice position was highly beneficial for visually comparing spatial correlations between different physical quantities.

B. What are inconvenient parts that can be improved?

1. Lack of Numerical Statistics: A major drawback is the absence of numerical values for key statistics (e.g., mean, variance). The GUI only displays PDF graphs, forcing users to export data to external software like Python for basic quantitative checks, which causes inefficiency.
2. No Point Probing: While general contour distributions are visible, the lack of a point probe feature to inspect exact values at specific coordinates through mouse click limited the ability to perform precise local analysis.

Appendix. Raw data tables used in this project

r (Distance)	$f(r)$ (Longitudinal)	$g(r)$ (Transverse)	D_{LL}	D_{NN}	D_{LLL}
0	1	1	0	0	0
0.05	0.996856	0.993017	0.043819	0.087743	-0.00495
0.1	0.988641	0.975442	0.157773	0.304503	-0.02995
0.15	0.974862	0.945115	0.348784	0.675967	-0.09421
0.2	0.955175	0.901387	0.625392	1.226295	-0.22584
0.25	0.935614	0.860553	0.893757	1.705384	-0.34802
0.3	0.910318	0.806392	1.246335	2.366984	-0.54608
0.4	0.856881	0.699903	1.988417	3.658067	-1.03544
0.5	0.797408	0.590058	2.823261	5.040754	-1.72214
0.6	0.735066	0.487136	3.712991	6.423723	-2.54743
0.8	0.627108	0.336033	5.204606	8.39756	-3.64765
1	0.523089	0.21314	6.702523	10.23067	-4.47756
1.25	0.41672	0.108424	8.183504	11.43806	-5.15948
1.5	0.337209	0.034681	9.272914	12.19923	-4.7318
1.75	0.278969	-0.00822	10.09068	12.83045	-4.07864
2	0.228967	-0.0282	10.8058	13.30146	-2.99861
2.25	0.180959	-0.02851	11.51207	13.40142	-2.06033
2.5	0.148665	-0.02495	11.97014	13.36396	-0.98907
2.8	0.136167	-0.02257	12.11533	13.41187	-0.62842
3.14	0.13171	-0.01977	12.25197	13.78507	-0.22915

References

[1] S. B. Pope, Turbulent Flows, Cambridge University Press, 2000.

[2] Dept. of Mech. Eng. (2025). Isotropic Turbulence DNS Data Viewer & Simulator [GUI software]. Yonsei University. *(MEU7300 Course Material)*